VORTEX SHEDDING AND INTERFACE OSCILLATIONS OF WIND-FORCED LIQUID DROPS

A Thesis

by

ROGER LOUIS SIMON, JR.

Submitted to the Office of Graduate and Professional Studies of
Texas A&M University
in partial fulfillment of the requirements for the degree of

MASTER OF SCIENCE

Chair of Committee,	Edward White
Committee Members,	Bonnie Dunbar
	Dion Antao
Head of Department,	Srinivas Vadali

May 2021

Major Subject: Aerospace Engineering

ABSTRACT

The conditions that lead to the depinning and runback of wind-forced liquid drops is an important problem in fluid mechanics that relates to aircraft ice accumulation and other situations. Multiple studies have examined wind-forced depinning but none have addressed how airflow and drop interface unsteadiness may be connected to depinning. Motivated by this, water drops ranging from 50 μL to 275 μL were placed on a horizontal, aluminum surface in a miniature wind tunnel and forced nearly to depinning using laminar wind flow. For each experiment, drop interface unsteadiness was captured using a high-speed camera while airflow fluctuations were measured using a hotwire anemometer. A synchronization technique was used in order to simultaneously measure drop oscillation and airflow unsteadiness. The data show that drop oscillation frequencies are independent of airflow speed but that the drop Bond number (the ratio of gravitational forces to surface tension forces) has a significant effect on drop oscillation frequency. Drop oscillation amplitude also increases markedly with freestream velocity. For the drops considered, the Strouhal number that characterizes unsteady airflow frequencies was found to have a range of 0.09 to 0.18. Lastly, a hemisphere versus water drop comparison concluded that the unsteady airflow frequencies are not affected by drop oscillation. These results suggest that while drop interface oscillation amplitude does depend on wind speed, there is not a coupling between drop interface unsteadiness and airflow unsteadiness in the drop wake.

DEDICATION

To my family, your unwavering support gives me the strength and drive to always push to new limits.

ACKNOWLEDGMENTS

I would like to give special thanks to my advisor, Dr. Edward White. Your warm spirit, guidance, and countless words of encouragement enabled me to achieve things that I did not think was possible. Thanks for always believing in me and never giving up. You have instilled valuable lessons in me over these past four years and I will cherish that.

I extend my deepest thanks to my family for your endless, unconditional love. To my dad, thank you for always remaining curious about my research and listening to me talk about the latest obstacle I was facing. To my mom, thanks for keeping me grounded when inevitable storms came. To my brother and sister, you both kept me focused on the things that truly matter.

To the one that makes all things well, my Lord and Savior Jesus Christ, I am forever grateful for your constant direction, unmerited favor, and mighty power. Without You, none of this would have been possible.

CONTRIBUTORS AND FUNDING SOURCES

Contributors

This work was supported by a thesis committee consisting of Professors Edward White and Bonnie Dunbar of the Department of Aerospace Engineering and Professor Dion Antao of the Department of Mechanical Engineering.

All work conducted for the thesis was completed by the student independently.

Funding Sources

Graduate study was supported by the National Science Foundation awards No. HRD-1810995 and CBET-1839103.

TABLE OF CONTENTS

Page

LIST OF FIGURES

FIGURE Page

1. INTRODUCTION

When a sessile liquid drop rests on a solid, horizontal surface in the presence of an incoming airflow, it may remain fixed in place or depin and proceed to move downstream. If the wind forcing is sufficiently low, the adhesive force existing at the liquid-solid interface will keep the drop pinned in its initial location. However, if the wind force ever exceeds the maximum adhesive force, the drop will undergo runback [2]. Depinning under wind forcing is pertinent to many applications. The process is relevant to heat exchangers [3], fuel cells [4], oil recovery [5, 6], and aircraft icing [7]. In these applications, liquid drops are subject to aerodynamic forces at the air-water interface. As a result, the drop adjusts its shape until, eventually, pressure and viscous stresses exceed adhesive forces at the contact line and cause the drop to dislodge from its initial location.

This is an interesting area of study because it focuses on the interaction between liquid- and gas-phase fluids. Predicting depinning limits, such as the wind velocity required to dislodge a particular drop, is challenging because interface oscillation is an unsteady phenomenon that tremendously complicates models of the behavior. The focus of this research will be centered on studying these dynamic processes at the instance right before the drop depins and begins to proceed downstream.

The aerodynamic drag forces acting on a drop is largely dependent on incoming flow velocity and drop frontal area (which is a function of drop volume and contact angle). Resistance to motion is provided by surface tension at the three-phase contact line. Contact angle hysteresis provides metastable drop configurations and the necessary criteria for drop depinning. As illustrated in Figure 1.1, the advancing contact angle, θ_a, is the maximum angle on the drop advancing side, while the receding contact angle, θ_r, is the minimum angle on the drop receding side. The intrinsic contact is θ_i; differences up to θ_a and θ_r are provided by surface roughness.

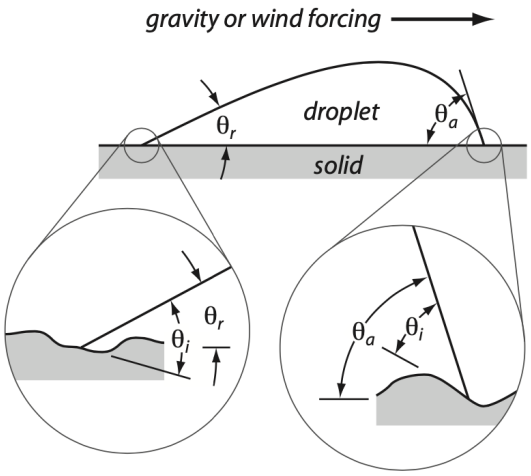

Figure 1.1: Contact angle hysteresis. Reprinted from Reference [1]

In the absence of any external forces and with a uniform contact angle, a drop would take the shape of a spherical cap. This is a consequence of surface tension. The Bond number is a standard indicator of whether surface tension is dominating over gravitational forces (which causes drops to spread). It is defined $Bo = \rho g h^2/\gamma$ where ρ is the liquid density, g is the acceleration of gravity, h is the drop height, and γ is surface tension. When the Bond number is small, surface tension dominates gravity forces and drops are shaped similar to spherical caps. When the Bond number is larger than one, drops begin to spread into the shape of a puddle.

When drops are acted on by weak wind forcing, they deform due to shear stress and pressure stress, acquiring a tear-shaped profile. If the incoming flow speed is high enough [8], airflow vortices will shed on the drop downstream side, leading to unsteady drag forcing on the drop. As the force varies, surface tension will behave as a restoring force and attempt to bring the drop back to its initial stable equilibrium point. The increase in drop frontal area will increase the drag force and this leads to an interface-shape oscillation.

Studying the effects of external flows on different types of bluff bodies has been of great interest for many decades now, but knowledge gaps yet remain. More specifically, useful

insight on the stability of water drops, consisting of theoretical, experimental, and computational perspectives, is still quite limited. A review of relevant literature on drop depinning, drop interface unsteadiness, and vortex shedding is presented with the aim to provide motivation of the current study to assess the physical reason for depinning of wind-forced liquid drops.

1.1 Drop Depinning

Some of the earliest work of drop depinning was by Bikerman [9] who studied the impact surface roughness has on drop depinning. Mahé et al. [5] experimentally investigated the adhesion process of a drop attached to a wall and its tendency to dislodge, influenced by a shear flow. They were able to measure the critical shear rate applied to the drop as a function of diameter. White and Schmucker [7] studied critical runback drop volumes for several different turbulent flow velocities and observed drop interface unsteadiness prior to depinning.

Milne et al. [2] sought to develop a way to systematically find the criteria necessary for drop depinning, by varying surface tension, air velocity, and drop area/shape on hydrophobic and hydrophilic surfaces. They found that the critical drop runback velocity is related to contact angle and drop size. This finding was later supported by Fan [10] who performed experiments which observed drop motion by applying a controlled shear flow and varying the type of fluid and surface. Fan proved that the critical velocity necessary for drop runback is related to the contact angle and drop size. More recently, White and Schmucker [11] observed that depinning always occurs at Reynolds numbers based on drop height associated with strong vortex shedding in the drop wake.

In all these efforts to provide a holistic understanding of drop depinning, little mention is made of potential coupling between the airflow and oscillating drop surfaces prior to drop depinning. It only answers the following question: what undeformed drop parameters are related to the velocity necessary for drop runback? However, large drop oscillations are observed [7] and are thought to play an important role [11]. This lack of knowledge inspires

the present study to provide insight on the fundamental, physical reason for depinning of wind-forced liquid drops.

Various computational studies have also been performed in order to describe the necessary conditions for a sessile drop to become dislodge. Durbin [12] derived an integro-differential equation defining the drop shape and found the critical Weber number as a function of contact angle hysteresis. Dimitrakopoulos and Higdon [13] conducted a series of numerical simulations to determine necessary conditions for drop displacement undergoing shear flows at low Reynolds number.

Schleizer and Bonnecaze [6] numerically studied the displacement of a two-dimensional drop immersed in a shear or pressure-dominated flow, neglecting inertial and gravitational forces. In more recent work, Seiler et al. [14] developed a model which predicts the capillary number associated with the undisturbed channel flow velocity at a wall normal distance of half the drop height.

A significant number of analytical models exist, but they are often limited to low Reynolds numbers and other simplifications such as small density differences between the drop and surrounding fluid, two-dimensional simulations, and simplified flow fields. This calls for the need of experimental data to explain this phenomenon.

1.2 Drop Interface Unsteadiness

Drop interface unsteadiness may affect when a drop depins due to possible resonance between the interface and airflow oscillations. Extensive research has gone into studying drop oscillation under different conditions. Studies of drop oscillation date to at least 1843, when Plateau first discovered this drop behavior, resulting from the breakdown of falling water streams [15]. The study of axisymmetric oscillations of constrained drops did not gain attention until much later. Rodot et al. [16] were the first to report experimental observations for a drop fixed to the end of a rod, forced to oscillate axisymetrically in a fluid with matching density. This was done in order to eliminate gravity effects and study oscillations restored by pure surface tension.

The experimental work by Rodot et al. inspired a numerous amount of researchers to develop numerical models to better explain this phenomenon. Strani et al. [17] were the first to conduct a mathematical analysis of constrained drop oscillations using Legendre polynomials from which they calculated eigenvalues and frequencies for various modes. They found that constraining the drop increases the frequency of oscillation for each mode compared to a free drop. The amount of increase is dependent on contact angle and mode number. Related analyses have been performed by many others [18–22].

Non-axisymmetric drop oscillations did not receive attention until the early 1980s. Following Rodot et al. [16], Bisch [23] observed non-axisymmetric oscillations of a constrained drop by laterally forcing a rod on which a drop was suspended in a matched density liquid. Bisch found that non-axisymmetric resonant modes have lower oscillation frequencies compared to axisymmetric modes.

Numerous researchers [20–22, 24] developed first-principles, infinite-summation equations to calculate eigenvalues and frequencies for non-axisymmetric modes of constrained drops. However, three-dimensionality of a drop increases complexities. Recent work by Sharma et al. [25] presented an analytical solution for the natural oscillation of an inviscid sessile drop with low-Bond number and arbitrary contact angle. They found that their model agrees well with experimental results reported in the literature. To assist with future mathematical models, Milne et al. [26] developed a framework to assist with analysis and categorizing drop oscillations.

Holistically speaking, work in understanding drop interface unsteadiness is vast. The work by Milne and company provided qualitative, some quantitative, insight on various types of drop oscillations, but majority of the research, however, is taken from a mathematical perspective, not experimental. More experimental efforts will need to be made in order to better understand drop oscillations at a physical level.

1.3 Airflow Vortex Shedding

Airflow unsteadiness may lead to be impacted by drop oscillation and these interactions could have a role in drop depinning. When the flow over a surface encounters a surface protuberance, unsteady vortices are often produced in the wake of the protuberance. These vortices have been a research topic for many years. Work by Möller is noted as the first to observe this instability [27]. Möller employed stereoscopic cinematography to track the flow behavior behind a sphere as it was being carried through water. He described this phenomenon as a system of vortices moving at an angle, linked together in a "vortex chain". This laminar-to-turbulent flow behavior motivated work by others [28–30] who established the necessary conditions needed to cause laminar-to-turbulent transition, using two- and three-dimensional elements placed in an initially laminar boundary layer.

Hot film anemometry techniques have been used to examine these fluctuations downstream of a spherical roughness element in a developing laminar boundary layer [31]. Klebanoff et al. [29] expanded on this research, using hotwire methods, and showed how a hemisphere protuberance creates vortex shedding under the certain conditions [32]. Hall [33] observed this instability for various types of small bluff-type bodies. Metzler is credited as the first to observe hairpin vortices in the wake of a hemisphere set in an initially laminar boundary layer [34].

Experiments conducted by Acarlar and Smith [8] studied the vortex-shedding conditions and characteristics generated in the separated wakes of hemispheres and half teardrops. These protuberances were individually placed on a flat plate with an initially laminar boundary layer. Flow-visualization techniques were used to distinguish the different segments of both the hairpin vortices and the secondary structures which they generate. They found that vortex shedding from a hemisphere shows a periodic behavior in the radius-based Reynolds number range of $Re_r = \rho U_\infty r/\mu = 120$ to 3400, where r is the hemisphere radius and height of the teardrop shape. They also discovered that a stationary horseshoe vortex is formed at the stagnation point and extends along the perimeter for the hemisphere case. When

the body was modified to a half-teardrop shape, the standing vortex was eliminated. The change in the structure of the unsteady hairpin vortices was negligible for what was considered. Much of their work has been the foundation for a quantitative perspective of hairpin vortices and, because of this, vortex shedding is considered to be well understood. Even though a majority of past work studied hairpin vortices generated behind hemispheres and other solid bluff bodies, it is expected this same knowledge can be translated for water drops.

1.4 Motivation and Research Objective

The history of experimental, theoretical, and computational work related to drop depinning suggests additional research is needed in order to better understand the drop stability problem. Specifically, the role of drop interface unsteadiness of wind-forced drops must be further explained.

The goal of this thesis is to provide a new way of studying the drop stability problem through the careful assessment of drop interface unsteadiness and airflow unsteadiness in the separated drop wake. The following question is addressed: Is there a coupling between drop interface unsteadiness and airflow unsteadiness? If so, does this promote drop depinning? To answer this question, the present research makes simultaneous measurements of the unsteady interface shape and airflow fluctuations for various drop shapes and sizes. Near-wake hotwire measurements and high-speed, side-view video of the drop interface are taken simultaneously.

2. EXPERIMENTAL SETUP AND PROCEDURE

2.1 Wind Tunnel Setup

The controlled flow over the horizontal surface on which the drops rest is provided by a small open-return wind tunnel originally developed by Schmucker [1]. The tunnel is shown in Figures 2.1 and 2.2. The tunnel starts with an inlet fairing that produces streamlined airflow into the tunnel. Just after the inlet fairing, a paper honeycomb with a length-to-diameter ratio of 4:1 is used to create uniform flow. Two metal screens with 30 wires per inch and 65% open area are placed slightly downstream of the honeycomb screen. The metal screens, placed 3.5 inches apart, are used to break down any large scale turbulence features before entering the test section. The airflow then accelerates through a 10-inch-long contraction. The contraction reduces the wind tunnel width from 8 inches to 2 inches.

The contraction shape is a fifth-order polynomial that has zero slope and curvature at both ends. To measure flow rate, a differential pressure is measured across the contraction using a 10V/5 Torr MKS 226A differential pressure transducer. A NI-USB 6211 data acquisition system records the transducer output data and custom LabVIEW software converts this to the contraction pressure difference. As described below, this pressure difference is used to calculate and control the wind speed in the tunnel.

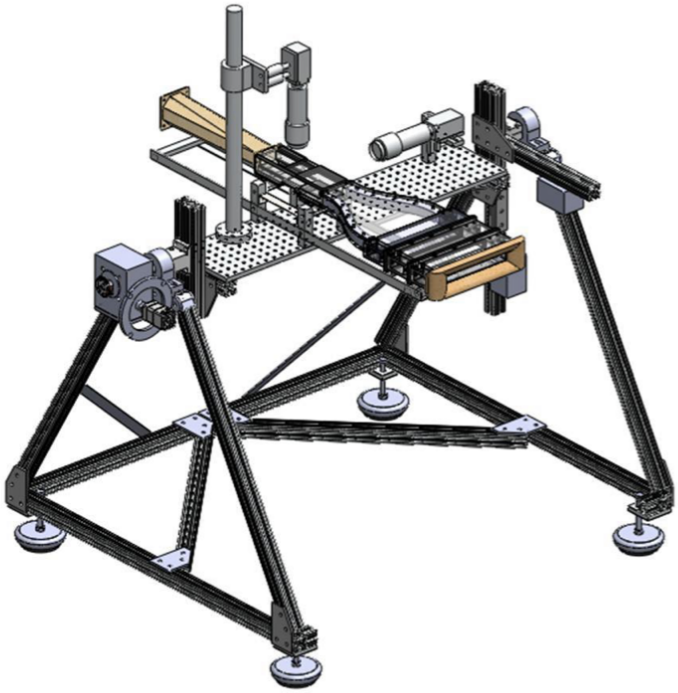

Figure 2.1: Schematic view of the wind tunnel used for vortex shedding and high-speed video experiments.

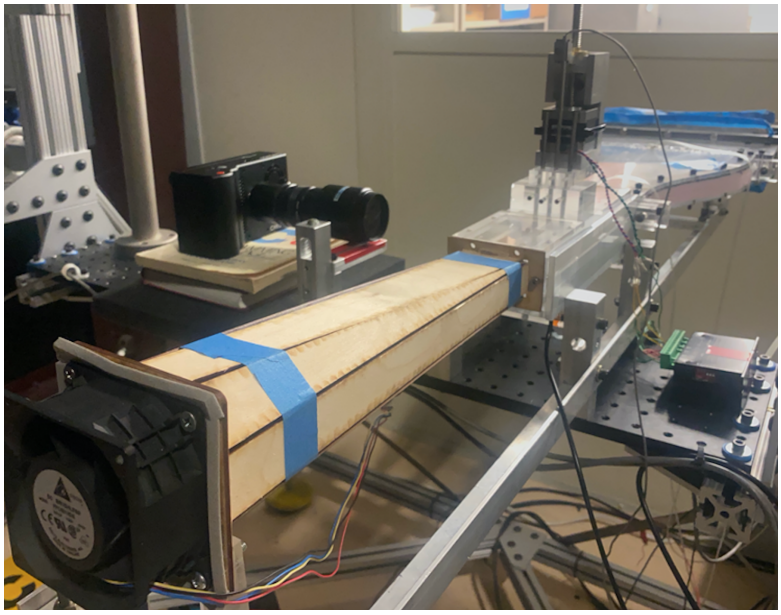

Figure 2.2: Physical image of wind tunnel used for vortex shedding and high-speed video experiments. The flow direction is top right to bottom left, out of the page.

Next, the flow proceeds through the test section that is 10 inches long by 1 inch tall by 2 inches wide. The tunnel sides and floor are made of acrylic and allow for good optical access. The top of the test section uses acrylic and 3D printed pieces of varying sizes to allow measurements to be taken at different downstream locations. At the midway point in the test section, an aluminum surface sample is placed in a machined rectangular slot. It is designed in such a way that allows the aluminum surface to be flush with the rest of the test section floor. Test drops are placed on the aluminum samples and the samples can be interchanged to provide different surface properties.

A rectangular-to-octagonal diffuser is located downstream of the test section. In order to discourage separation and upstream propagation of unsteadiness, the diffuser is constructed with a 5.5° half angle. Finally, a 80 mm Delta axial fan is connected at the end of the diffuser and is what draws flow through the tunnel. The fan speed is controlled by using the pulse-width modulation (PWM) technique.

To control wind speed in the test section, a feedback loop between the fan speed and the contraction pressure difference is implemented. A LabVIEW routine takes in a user-requested freestream velocity. This target velocity is compared to the current actual velocity estimated from the contraction pressure difference. The contraction pressure difference to test-section velocity calibration was established using a Pitot tube in the center of the test section attached to a 10V/10 Torr MKS 226A pressure transducer. This pressure reading was considered to be representative of the tunnel freestream velocity using Bernoulli's equation. The pressure transducer reading across the contraction is proportional to the Pitot tube pressure difference and a calibration constant was found that relates the values. The calibration constant was placed into the LabVIEW subroutine that converts pressure to velocity. The program then communicates with the fan through PWM input whether to increase or decrease fan speed. Once the current velocity is within a tolerance of 0.1 m/s, the fan will remain constant but continues to be adjusted as needed through each experiment.

2.2 Hotwire Setup

While the contraction pressure difference can be used to control the overall wind speed, a different instrument is needed for unsteady, spatially resolved measurements. With their excellent spatial resolutions and ability to sample at high frequencies, constant-temperature hotwires are ideal sensors for measuring laminar and turbulent flows. As shown in Figure 2.3, a hotwire is constructed with delicate precision.

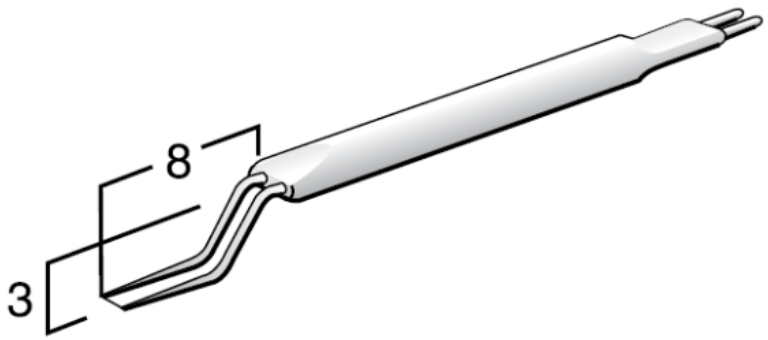

Figure 2.3: Hotwire schematic *(Dantec Dynamics)*
Dimensions in mm. Prong spacing is 1 mm. Typical wire diameters are 2.5 or 5 μm.

Constant-temperature hotwires operate on the principle that the temperature of a small sensor wire is maintained constant using closed-loop control. By placing a heated wire in the path of the incoming airflow, there is a heat loss to the colder flow. Measuring the heat loss provides a velocity measurement. The electrical resistance of the wire is a function of its temperature and heat loss is measured by measuring the voltage required to maintain constant resistance and, by extension, a constant temperature.

The voltage required to provide the current is a function of the heat transfer rate, which is a function of fluid velocity. Assuming T_{air} remains constant, which was the case during

the time of this research, King's Law states [35] that the voltage and velocity is related by the function $U = k1(E^2 - {E_0}^2)^n + k2(E - E_0)^{\frac{1}{2}}$ where $k1$, $k2$, and n are constants that are found by performing a daily calibration. The exponent n is approximately equal to 2. E_0 is the hotwire voltage at 0 m/s when heat loss is due only to natural convection and E is the voltage across the hotwire required to maintain temperature when $U > 0$. Calibration is done by slowly increasing the velocity from 0 to 18 m/s and recording the hotwire voltage and freestream velocity at discrete points, sampled at 2 kHz for 2 seconds. A fit is then applied to the data using the Levenberg-Marquadt nonlinear least squares algorithm [36]. Figure 2.4 shows a typical calibration result. In order to keep the sensor wire safely secured, the set of straight prongs was carefully placed in a hotwire holder. A BNC cable was attached to the holder, transferring output voltage values to a hotwire anemometer.

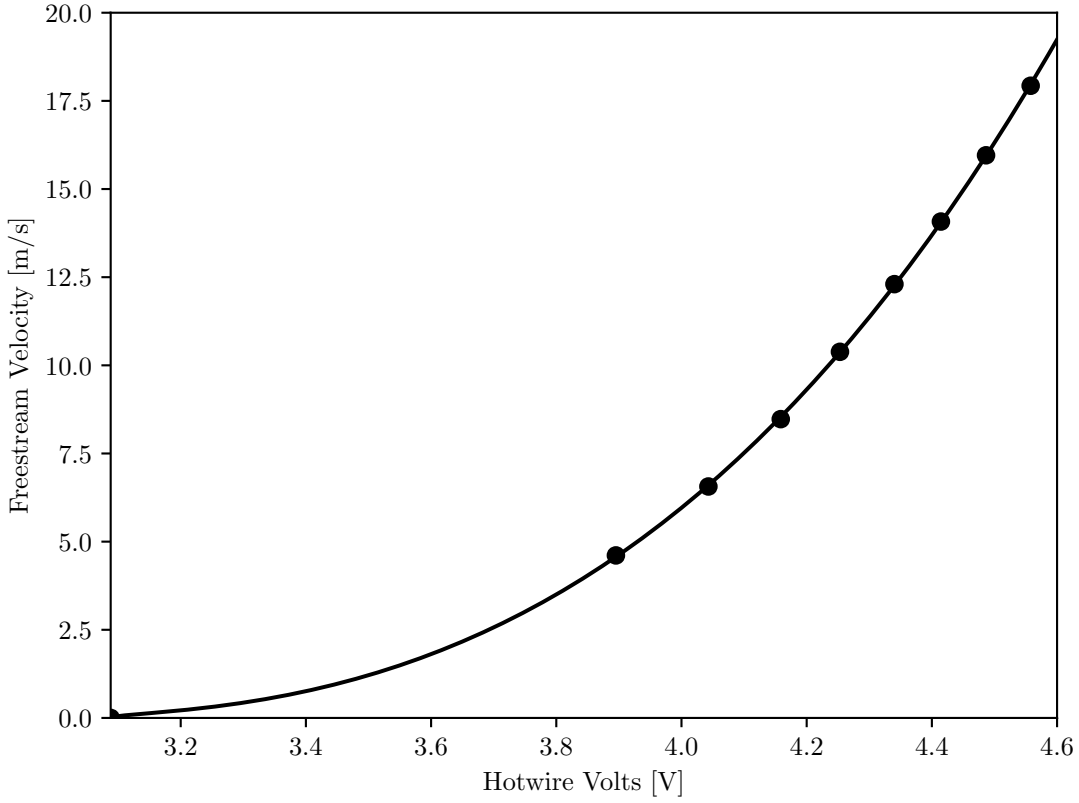

Figure 2.4: A hotwire calibration result

The vertical position of the hotwire in the tunnel is controlled using a stepper motor attached to a fine-pitch lead screw. The combination provides automatic position control with 1.25 μm resolution. The motor driver receives forward and reverse commands from a LabVIEW subroutine. The hotwire data is collected through National Instruments USB-6211 data acquisition system.

2.3 High-Speed Camera Setup

A Chronos 1.4 high-speed camera was used to capture dynamic drop interface motion. A Navitar Zoom 7000 camera lens with a focal length range of 18 - 108 mm was used. The camera was placed on a mounting system that allowed the lens to remain level with the aluminum substrate. The camera was set up to record in segmented mode, which allows multiple recordings to be stored in a single video file. Videos were recorded at 500 frames per second for 2 seconds, a resolution of 1280x1024, and an exposure time of 491μs. Analog or digital gain was not applied.

Figure 2.5 shows an example of a single frame output. In this image a stationary 75 μL drop is visible at the left, acted on by a 7.9 m/s airflow from left to right. The hotwire at the right is positioned 1.19 mm above the aluminum substrate. The bottom of the frame provides information related to when the image was taken: 705/1000 is the frame number of the particular segment, sg=3/5 is the current segment number out of total number of segments, and T=1.41s is the amount of time after the trigger was received to record the image.

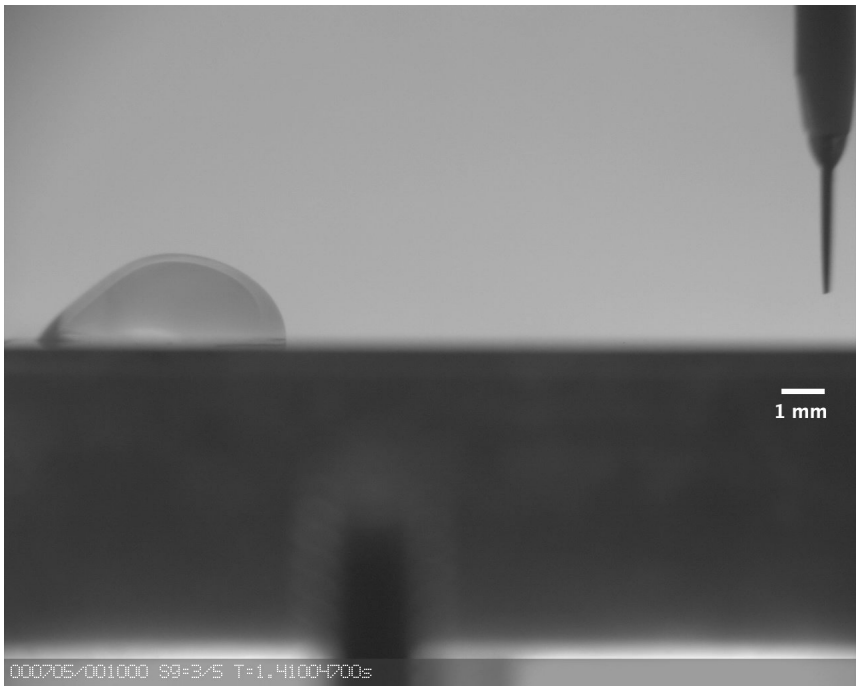

Figure 2.5: A single frame output from high-speed camera.

Many approaches could be devised for measuring drop interface unsteadiness. In this work, variations in average pixel intensity in a region including a portion of the interface silhouette are used. Using the drop apex and the advancing contact point as reference, a bounding box was manually placed on the first video frame for each recording segment. For example, in a typical experiment, a trigger would occur at 4 m/s, 6 m/s, and 8 m/s and a bounding box would be manually applied at the first frame of each speed. Figure 2.6 shows this box in a particular case.

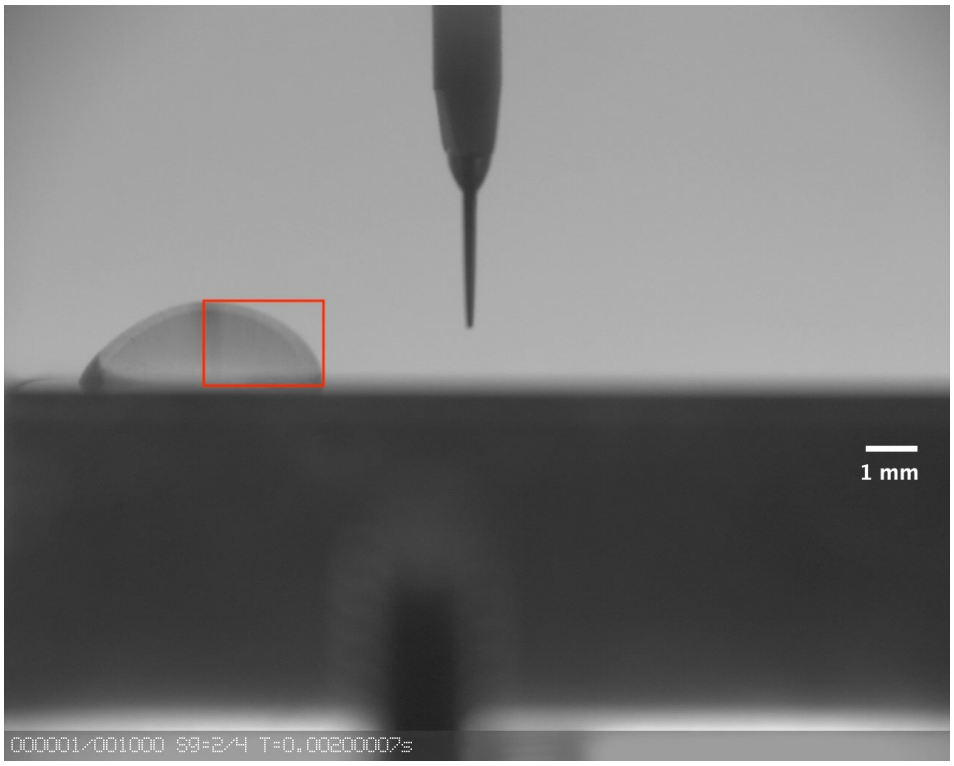

Figure 2.6: Initial bounding region used to set max limits on area of interest

Next, the initial box in Figure 2.6 was subdivided into four equal parts and the top left quadrant was used for analysis. Figure 2.7 shows the analysis region. Important to stress, this location will not move throughout the remaining frames.

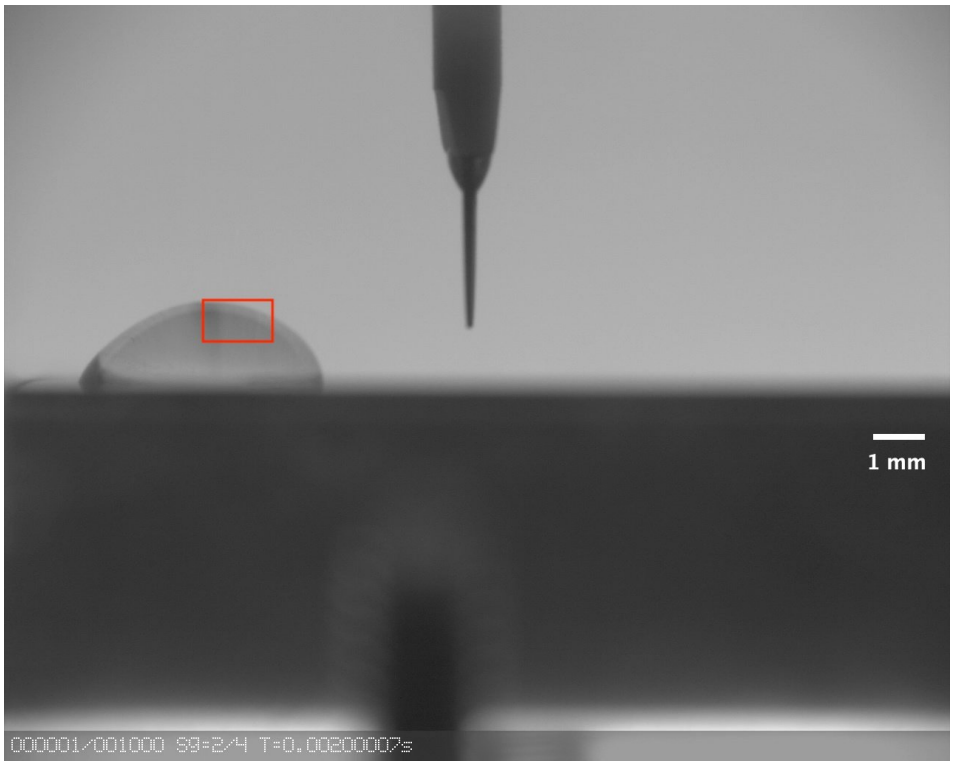

Figure 2.7: Analysis region used to calculate drop surface oscillation frequency

Finally, the average pixel intensity in the analysis region is calculated for each frame. Broadly speaking, the analysis will show an average darker intensity when the drop oscillates to the right and a lighter intensity as it oscillates left. The magnitude of these changes will increase with oscillation amplitude.

2.4 Synchronization Technique

To correctly understand potential interactions between airflow and drop unsteadiness, it is essential to record hotwire and high-speed video images simultaneously. To achieve this, a careful approach to triggering data acquisition was developed. At the beginning of a sample, the data acquisition system sends a voltage signal (i.e., a trigger) to the camera using an analog output channel (AO0). At the same time, simultaneously, a second analog output channel (AO1) sends a trigger to a digital input channel that initiates hotwire acquisition initiation. This setup ensures that the high-speed video and hotwire data were acquired

simultaneously. Howire data was saved on the local computer, while high-speed video was saved on camera RAM and later moved to a computer for processing using an SD card.

2.5 Test Procedure

The first step to conduct an experiment is to clean the aluminum surface with acetone, removing leftover water debris or dust particles from the previous experiment. After the surface dries, a drop is measured using a graduated Hamilton syringe, with an uncertainty of 1 μL. The water volume is carefully applied to the surface with a near-circular contact line. The hotwire setup is then placed into position behind the drop. The camera recording button is pressed and this instructs the camera to remain in standby mode until a trigger is received. Next, the main LabVIEW code is executed. It is configured to conduct the entire experiment without user intervention. The code takes measurements at pre-specified, increasing freestream speeds. The contraction pressure difference is monitored continuously. Simultaneous hotwire and video recording is triggered when the wind velocity reaches a stable set point. These set points were determined using preliminary tests that determined anticipated runback velocities as a function of drop volume. The camera recording button is pressed a final time to conclude its standby status. The high-speed video is saved as a .mp4 file onto an SD card and the hotwire data is saved onto a hard drive. This process is repeated for all considered drop volumes. Both sets of data are later processed using custom Python code.

3. BASIC STATE ASSESSMENT

Before studying drop interface unsteadiness and airflow fluctuations, the wind tunnel basic state must be understood. The overall objective of assessing the basic state was to ensure that laminar flow is achieved in the same area of where the drop is placed. Boundary-layer profiles, turbulence intensity levels, and boundary-layer thicknesses for different operational freestream speeds were carefully studied during this phase of the research.

Figure 3.1 shows the result from a boundary-layer scan at 3.55 m/s. The hotwire was placed at the midway point along the test section, putting it in close proximity of where a drop would be. An average of the first five points was used to denote the freestream speed. In this example, it would be 3.55 m/s. The local flow velocities were normalized by this value. To prevent the hotwire from hitting the wall, the hotwire would stop traversing after the local velocity is under a certain threshold value. In order to find the wall location, a linear extrapolation of the last five points was used. The black line plot shows the boundary layer. Length scales ranging from eddies to 5.0μm or less could be measured. The blue squares highlight turbulence intensity levels u'_{rms}/U_∞ throughout the profile where u'_{rms} is the root-mean-square of velocity fluctuations. Turbulent intensities between 0.4% and 0.8% are observed. These are sufficiently low to be considered laminar.

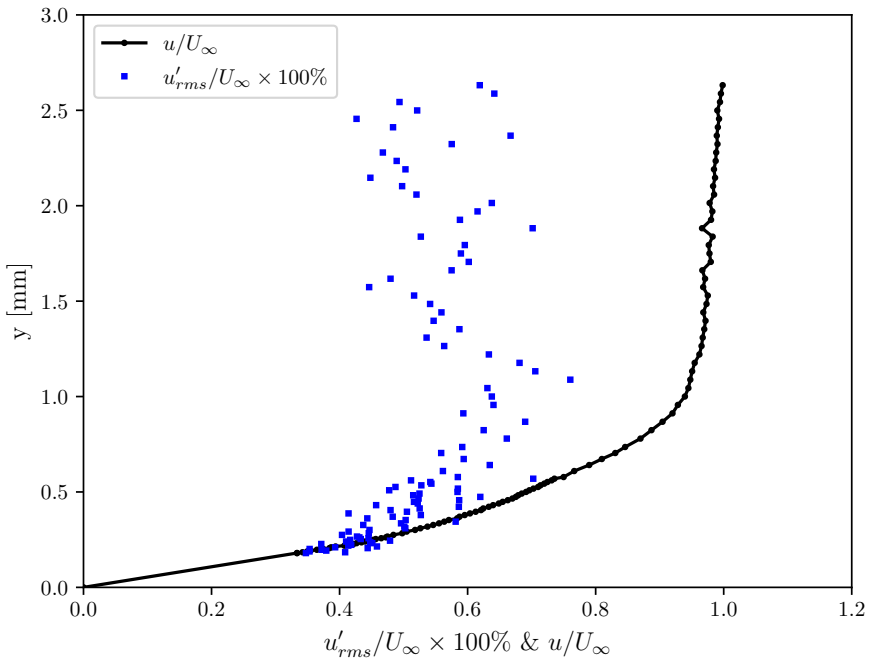

Figure 3.1: u'_{rms} and boundary-layer profile at 3.55 m/s

Profiles for multiple freestream speeds are shown in Figure 3.2. As flow speed increases, the shear layer thickness decreases, as expected. The turbulence intensity levels seem to reach a maximum value of 1.2% at 5.83 m/s. Overall, the velocity fluctuations are considerably low across all considered flow speeds.

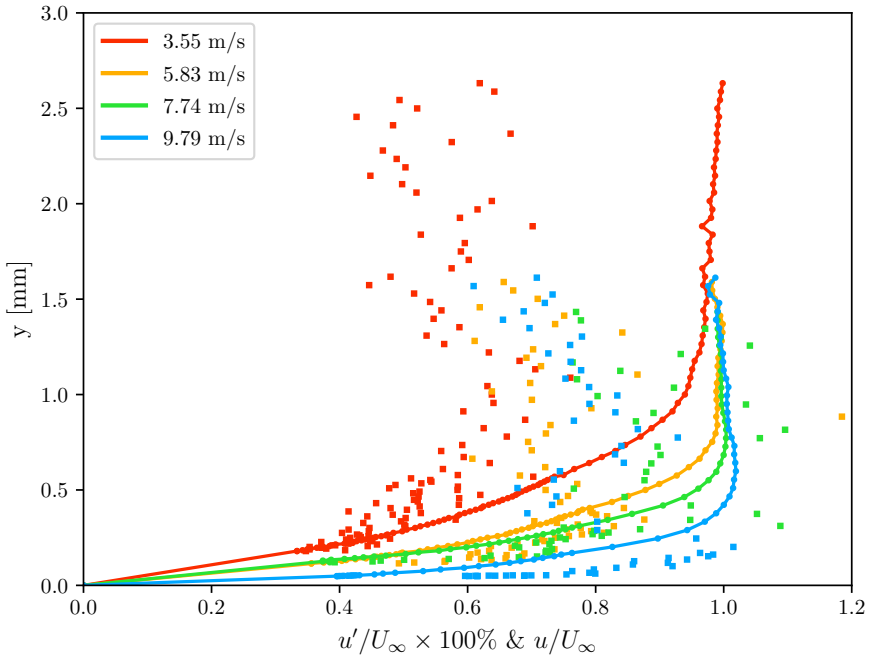

Figure 3.2: Mean and fluctuating boundary-layer velocity profiles for various freestream speeds

These boundary-layer profiles are self-similar and can be represented as a single function $u/U_\infty = f(y/\delta^*)$ where δ^* is the boundary-layer displacement thickness. This can be seen in Figure 3.3. The displacement thickness is defined

$$\delta^* = \int_0^\infty (1 - \frac{u}{U_\infty})\,\mathrm{d}y. \tag{3.1}$$

This self-similar curve is consistent with past work conducted using this particular wind tunnel [1]. Figures 3.4 and 3.5 highlight the consistency of the wind tunnel for displacement thickness, δ^*, and momentum thickness, θ. The momentum thickness is defined

$$\theta = \int_0^\infty (\frac{u}{U_\infty})(1 - \frac{u}{U_\infty})\,\mathrm{d}y. \tag{3.2}$$

The ratio of these thicknesses is called the shape factor, defined $H = \delta^*/\theta$. As shown in Figure 3.6, the mean shape factor lies roughly around 2.3 which is to be an acceptable level

for somewhat accelerated laminar flow.

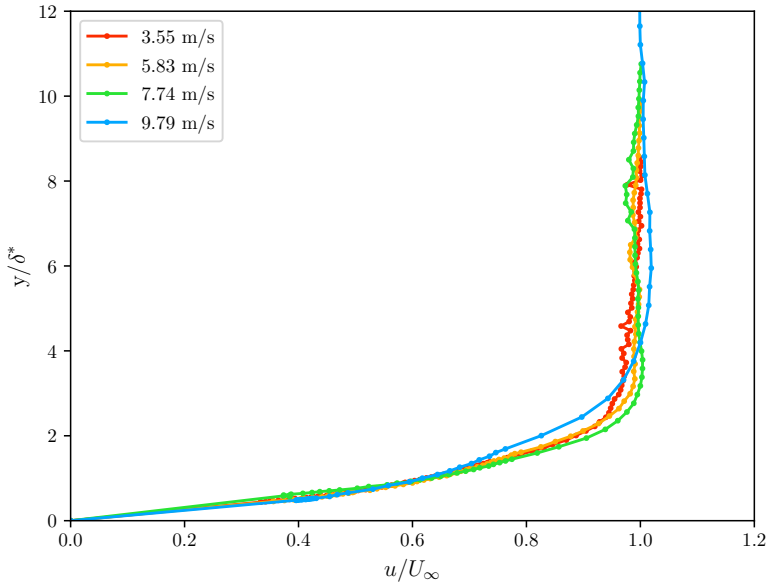

Figure 3.3: Normalized boundary-layer profiles for various freestream speeds

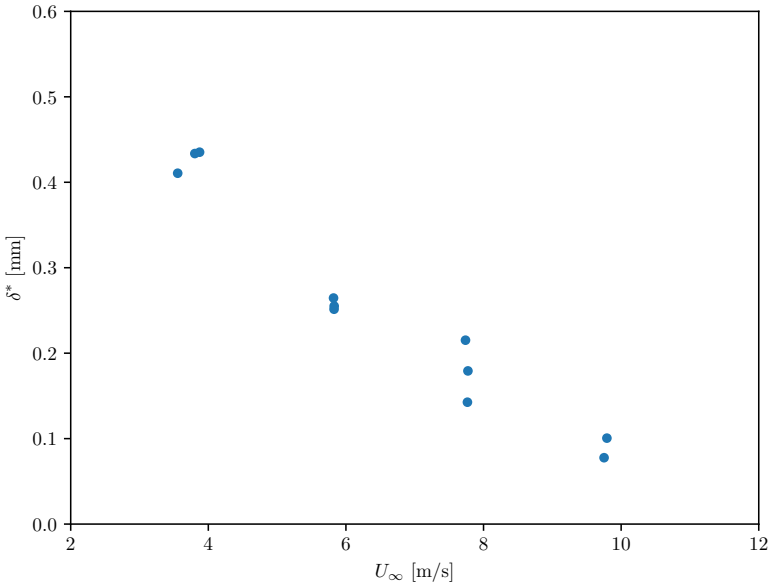

Figure 3.4: Displacement thickness for various freestream speeds

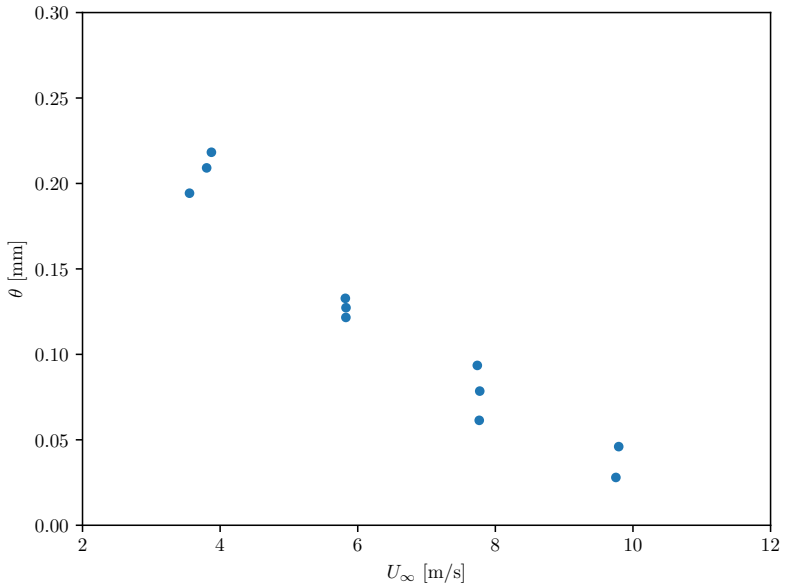

Figure 3.5: Momentum thickness for various freestream speeds

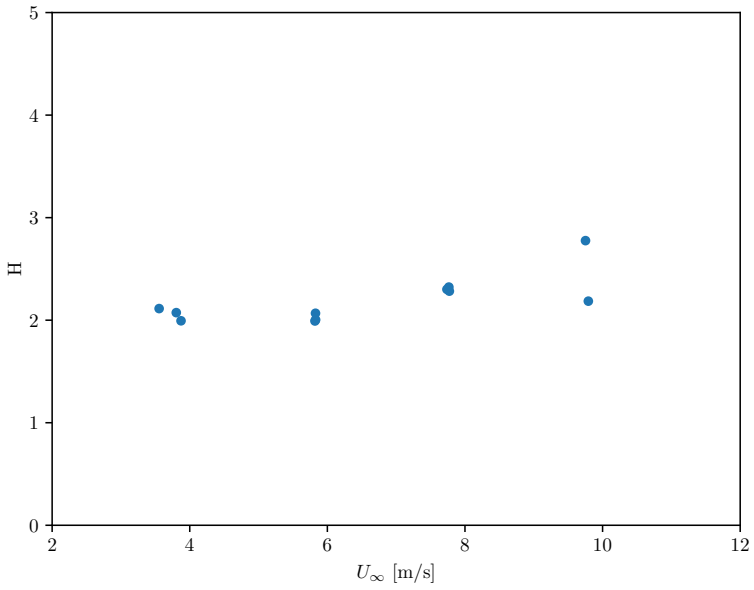

Figure 3.6: Shape factor for various freestream speeds

Besides simply noting low values of u'_{rms}, it is important to understand the frequency

content of the velocity fluctuations. Figure 3.7 show the u′ power spectra obtained at max u'_{rms} location for four freestream speeds.

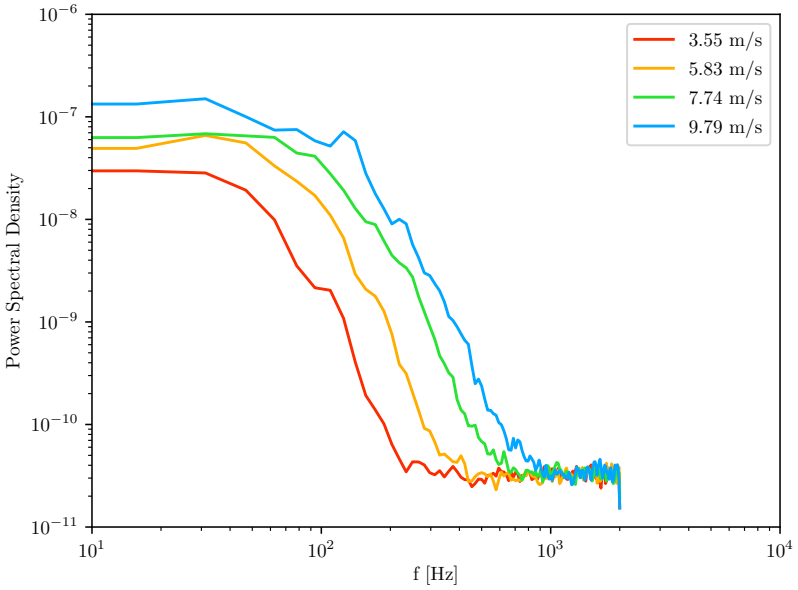

Figure 3.7: Power spectral density for various freestream speeds

The figures shown in this chapter provide clear evidence that the basic state flow has an acceptable behavior for drop depinning experiments. Because the flow is laminar, any unsteady frequencies will be the result of the air/drop interaction, not inflow turbulence. So, the research questions, "Is there a coupling between drop interface unsteadiness and airflow unsteadiness? If so, does this promote drop depinning?" can be assumed that the drops are subjected to an initial laminar flow.

4. RESULTS

The primary goal of this thesis is to investigate whether drop depinning is related to potential coupling between near-wake airflow unsteadiness and drop interface oscillation. In order to achieve this, simultaneous measurements of both phenomena are made and data is analyzed in the time and frequency domain. To see what effect interface oscillations have on airflow unsteadiness, comparisons between solid hemispheres and similarly sized water drops were also made.

4.1 Time-Domain Analysis

Drops ranging from 50 μL to 275 μL were placed on the aluminum surface and forced to near-runback conditions by increasing wind velocity in a stepwise fashion. The average pixel intensity indicating drop interface unsteadiness and hotwire voltage data indicating airflow velocity were both analyzed as a function of time. The high-speed camera and hotwire were sampled at a rate of 500 Hz for 2 seconds and 4000 Hz for 2 seconds, respectively. Figures 4.1 and 4.2 show the relationship between the two data sets for a 50 μL and 100 μL water drops. The units of both signals are arbitrary but scales are consistent between figures. Most notably, air velocity fluctuations are a substantially higher frequency than the drop interface unsteadiness.

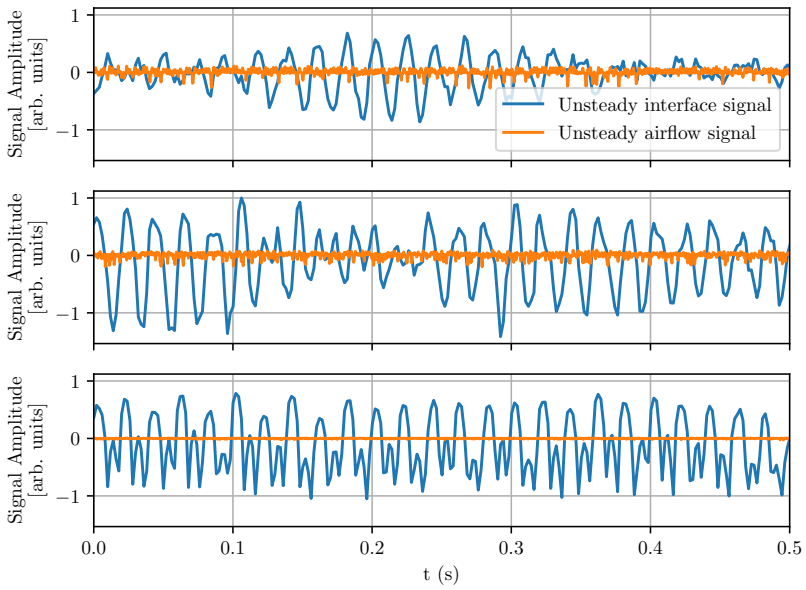

Figure 4.1: Time signals for a 50 μL water drop leading to near runback. The top plot $U_\infty = 5.9$ m/s. The middle plot $U_\infty = 7.9$ m/s. The bottom plot $U_\infty = 9.9$ m/s.

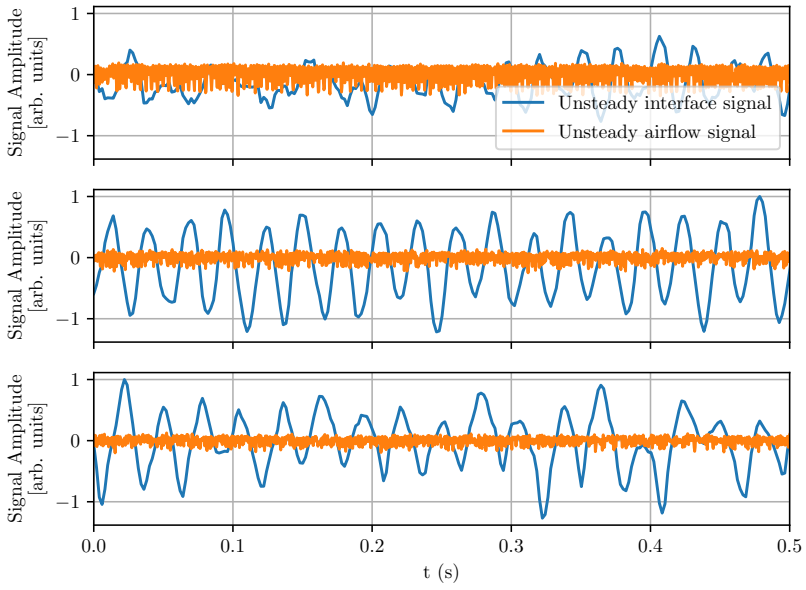

Figure 4.2: Time signals for a 100 μL water drop leading to near runback. The top plot $U_\infty = 5.9$ m/s. The middle plot $U_\infty = 7.9$ m/s. The bottom plot $U_\infty = 9.9$ m/s.

4.2 Frequency-Domain Analysis

The plots above show much higher unsteady frequencies for the airflow than the drop interface. To investigate this, fluctuation power spectra were generated using Welch's method [37]. As an example—using Figure 4.3 as reference—Figure 4.4 shows that for a 5.9 m/s wind speed, the first peak interface oscillation frequency of a 50 μL drop is found to be roughly 25 Hz and the remaining peaks up to the fifth are integer multiples of 25 Hz. The sixth peak frequency occurs at approximately 210 Hz. The multiple frequencies in the power spectrum is an indicator of drop oscillation unsteadiness. The first peak vortex shedding frequency in the drop's wake is 250 Hz - a 10 times difference from the first peak interface oscillation frequency. The second and third peak interface oscillation frequencies occur at 500 and 1000 Hz, respectively. As seen in the time domain, airflow unsteadiness is a much faster process than drop interface unsteadiness. However, the drop's presence generates periodic airflow unsteadiness due to the flow inability to remain attached, separating just downstream of the apex. Figure 3.7 and Figure 4.4 at roughly 6 m/s show that the presence of the drop causes an increase in airflow unsteadiness amplitude.

As the freestream speed increases to 7.9 m/s, using Figure 4.5 as reference, Figure 4.6 shows that the peak interface oscillation frequencies are consistent with what was observed at 5.9 m/s. A slight increase in amplitude can be seen as well. The first peak vortex shedding frequency increases to 400 Hz and no other peaks are observed in this power spectrum. Important to note, a slight increase in amplitude is evident. This proportional relationship between velocity and amplitude is observed for all drop sizes. Finally, with Figure 4.7 as reference, Figure 4.8 shows the same peak interface oscillation frequencies as the previous two speeds. The higher peak frequencies are more clear as well. The flow is considered to be turbulent at this particular hotwire location and vortex shedding frequency can not be determined. Nonetheless, for a 50 μL drop, the airflow appeared to not have an influence on interface oscillation frequency, only amplitude. Results for different hotwire locations will be discussed shortly.

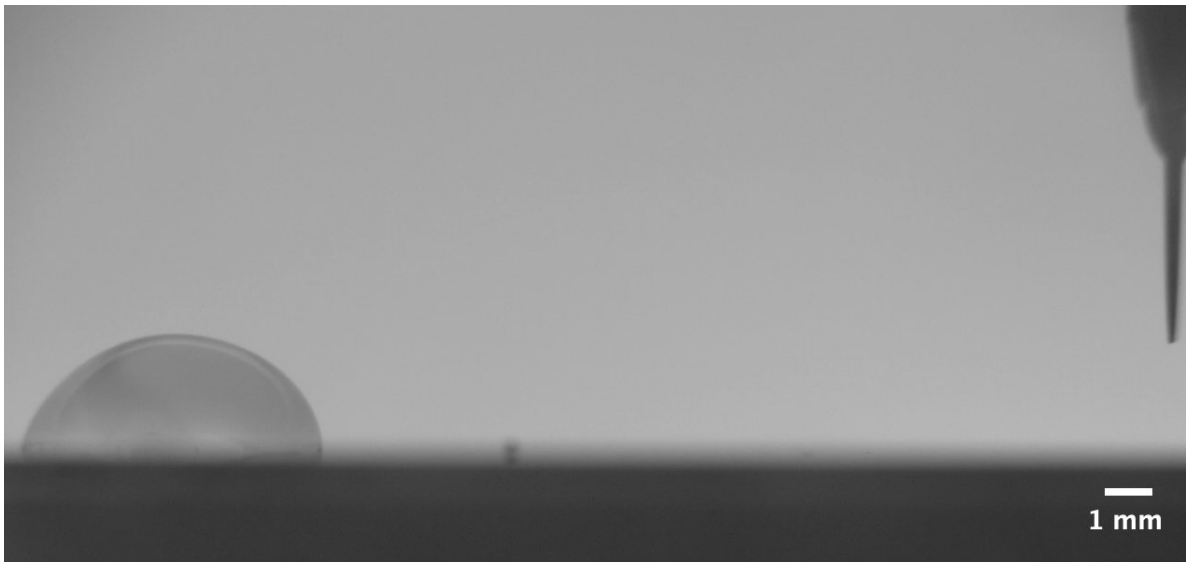

Figure 4.3: Shape of 50 μL water drop at 5.9 m/s and hotwire location relative to drop advancing side

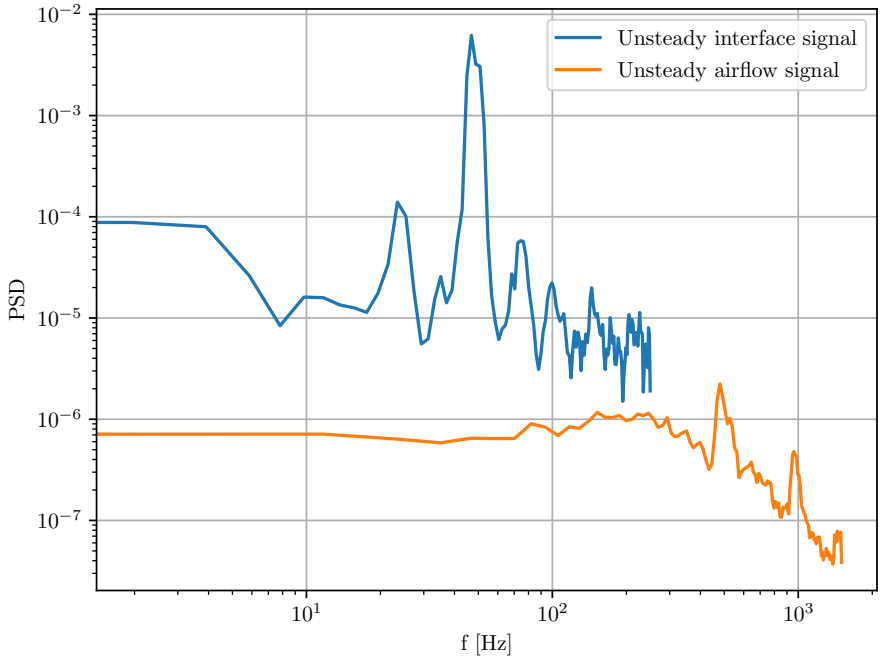

Figure 4.4: Unsteady signal power spectra for a 50 μL water drop and wake flow, $U_\infty = 5.9$ m/s.

Figure 4.5: Shape of 50 μL water drop at 7.9 m/s and hotwire location relative to drop advancing side

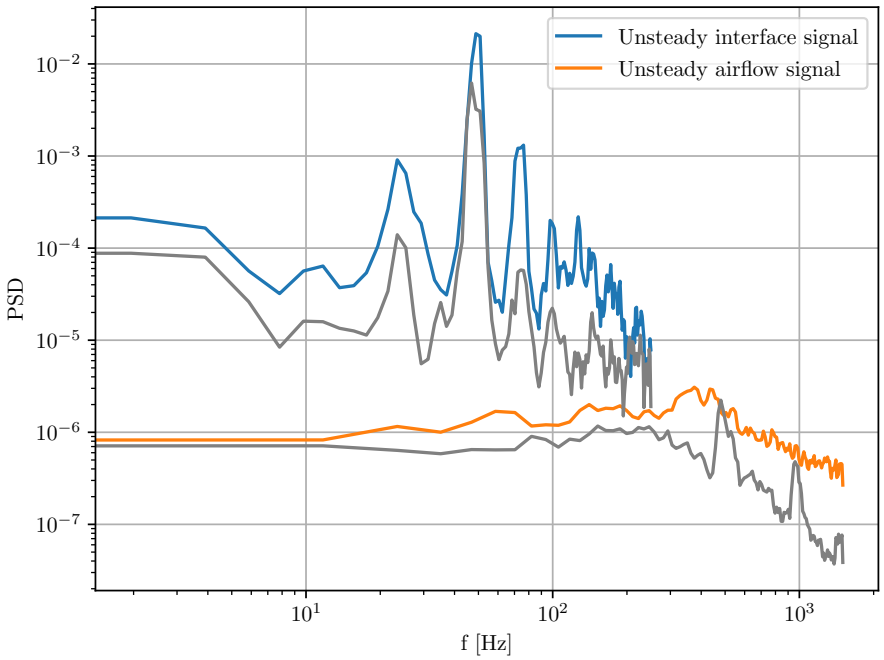

Figure 4.6: Unsteady signal power spectra for a 50 μL water drop and wake flow, Colored curves $U_\infty = 7.9$ m/s. Solid gray curves $U_\infty = 5.9$ m/s from Fig. 4.4.

Figure 4.7: Shape of 50 μL water drop at 9.9 m/s and hotwire location relative to drop advancing side

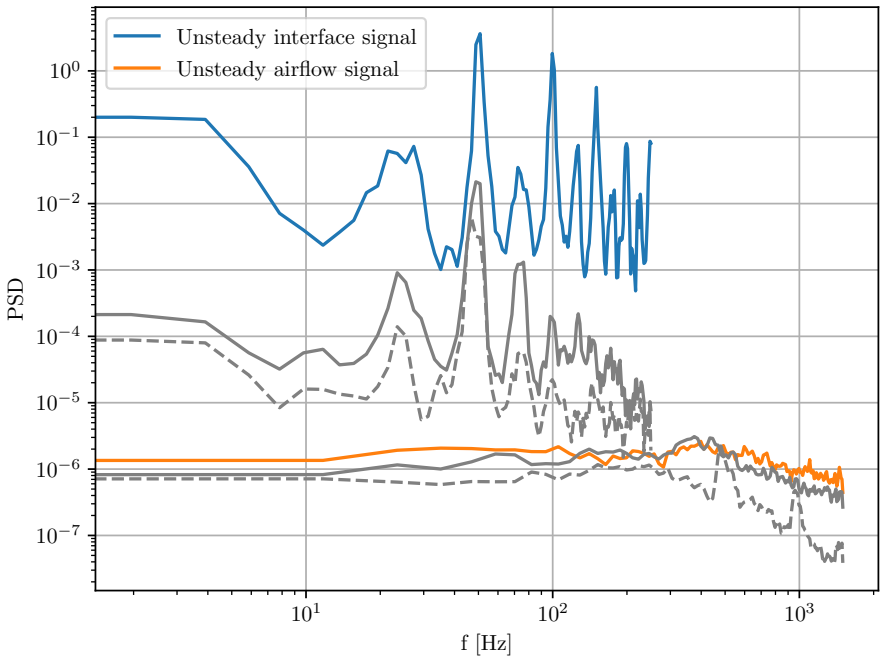

Figure 4.8: Unsteady signal power spectra for a 50 μL water drop and wake flow, Colored curves $U_\infty = 9.9$ m/s. Solid gray curves $U_\infty = 7.9$ m/s from Fig. 4.6. Dashed gray curves $U_\infty = 5.9$ m/s from Fig. 4.4.

At the same hotwire location as previously, Figure 4.9(a) at $U_\infty = 5.9$ m/s shows that the first peak interface oscillation frequency for a 75 μL drop occurs at 20 Hz, peaks up to the fourth one are integer multiples of 20 Hz, and the fifth peak occurs at approximately 90 Hz. Comparing to the 50 μL drop, these frequency values are smaller. The first four peak vortex shedding frequencies occur at 250, 450, 700, and 900 Hz. Similar to the 50 μL drop case, the drop interface is oscillating at a much slower pace compared to the airflow unsteadiness process. Also, the proportional relationship between airflow speed and amplitude is still observed. As volume increases, the interface oscillation frequency is expected to decrease because at the instance of when pressure drops in the near wake, the drop will propagate upstream but will do so at a slower rate due to its increased size. This trend can be seen in Figures 4.9(b-d).

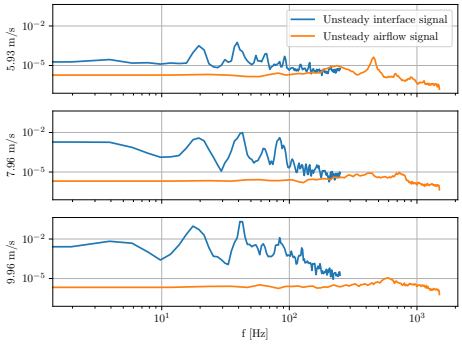

(a) 75 μL water drop

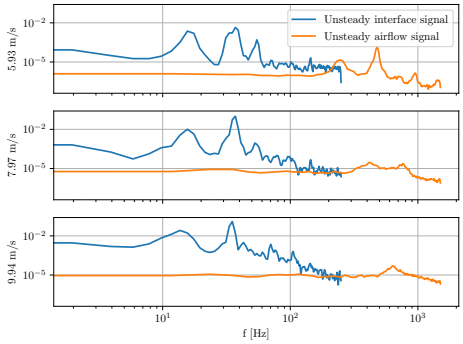

(b) 100 μL water drop

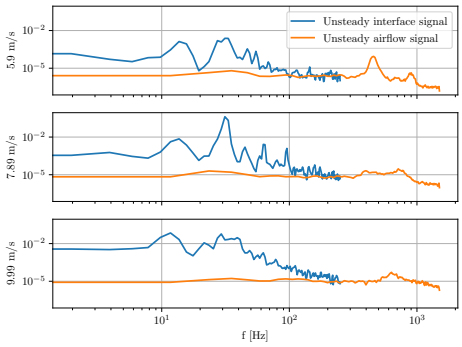

(c) 125 μL water drop

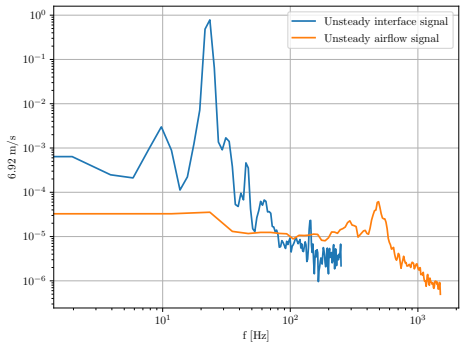

(d) 275 μL water drop

Figure 4.9: Unsteady signal power spectra for various drop volumes. The y-axis label indicates freestream speed.

As shown in Figure 4.10, drop volume up to 150 μL seems to have a significant influence on oscillation frequency, decreasing by a factor of 2. The effects are small past the 150 μL threshold. The second peak frequency was found to be twice the value of the first peak frequency. From a non-dimensional perspective, Figure 4.11 shows that once Bond number $Bo = \rho g h^2/\gamma$ exceeds one, interface oscillation frequency remains constant. Therefore, drop oscillation frequency is strongly dependent on surface tension forces dominating gravity forces. Figure 4.12 shows a linear relationship found between Reynolds number $Re = U_\infty x/\nu$ and Strouhal number $St = fT/U_\infty$ - both based on initial drop height - for the water drops considered.

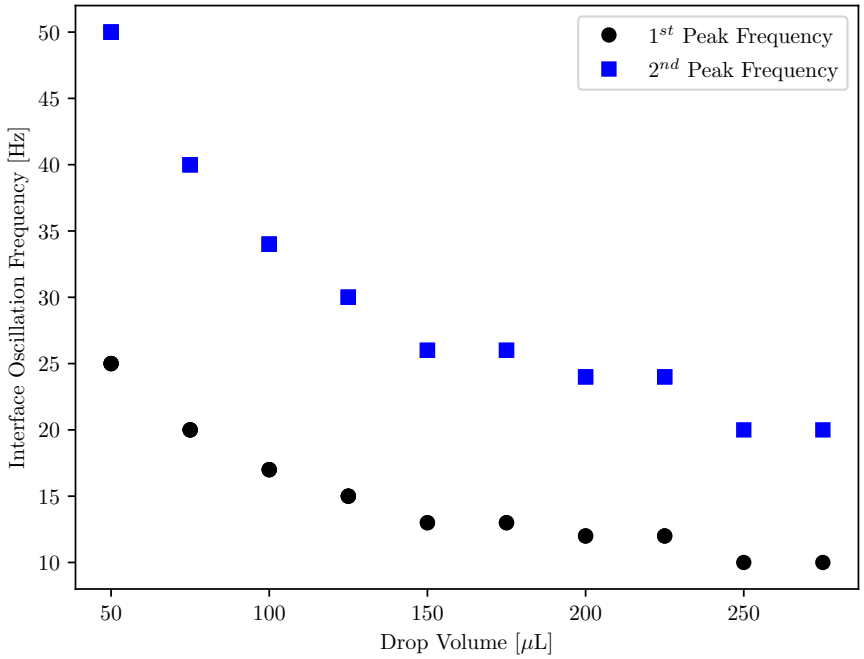

Figure 4.10: Interface Oscillation Frequency vs. Drop Volume

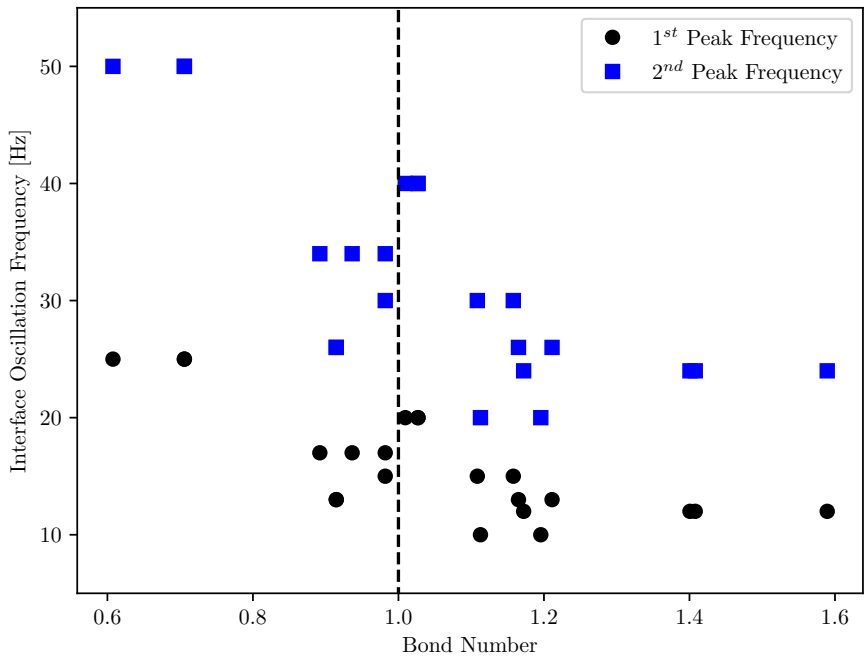

Figure 4.11: Interface Oscillation Frequency vs. Bond Number

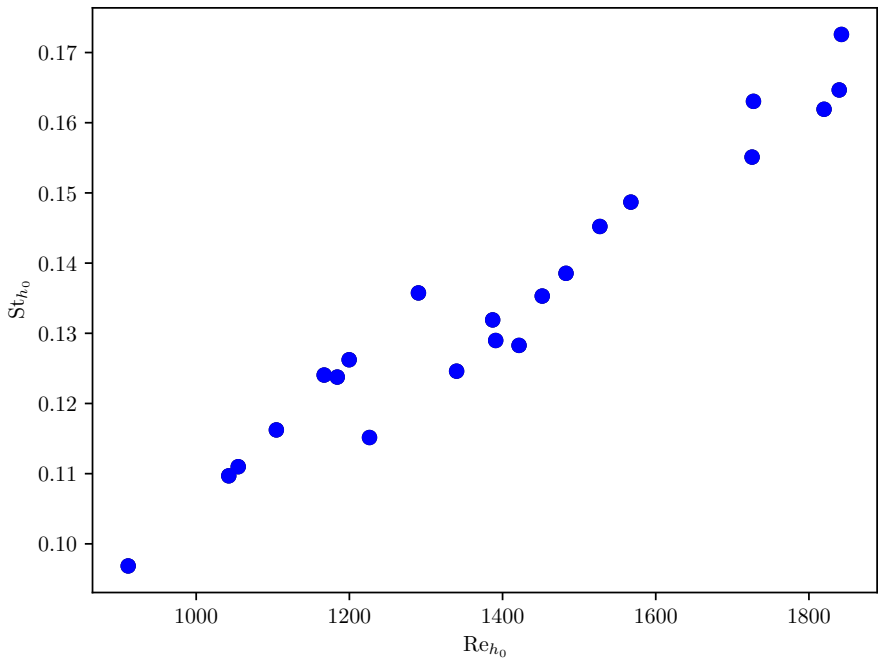

Figure 4.12: Strouhal Number vs. Reynolds number plot. Both parameters are based on initial drop height.

The hotwire was moved closer to the drop advancing side in order to see the effect its location has on the results. It was found that if the hotwire was too close to the drop, vortex shedding frequency information is lost. This is due to the hotwire being positioned in the wake region where dynamic pressure is substantially low. Figures 4.13-4.16 can be used to compare with the previous case discussed. Using Figure 4.17 as reference, Figure 4.18 shows indication of the hotwire being placed in the wake region. However, from what can be seen, the velocity and amplitude proportional relationship is evident as before. Also, interface oscillation frequencies are consistent with was presented earlier. This means that a drop is unaffected by where the hotwire is located but not vice versa, establishing more confidence in oscillation frequency values. Nonetheless, in order to recover substantial frequency content, conclusions were made based on the hotwire location presented at the beginning of this section.

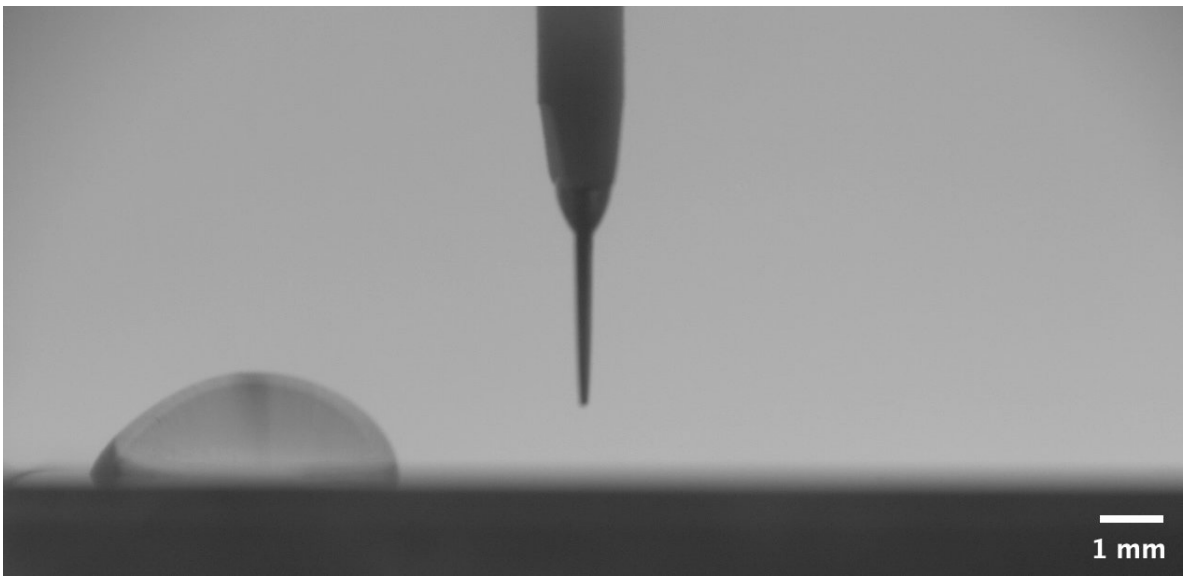

Figure 4.13: Shape of 50 μL water drop at 5.9 m/s and hotwire location relative to drop advancing side.

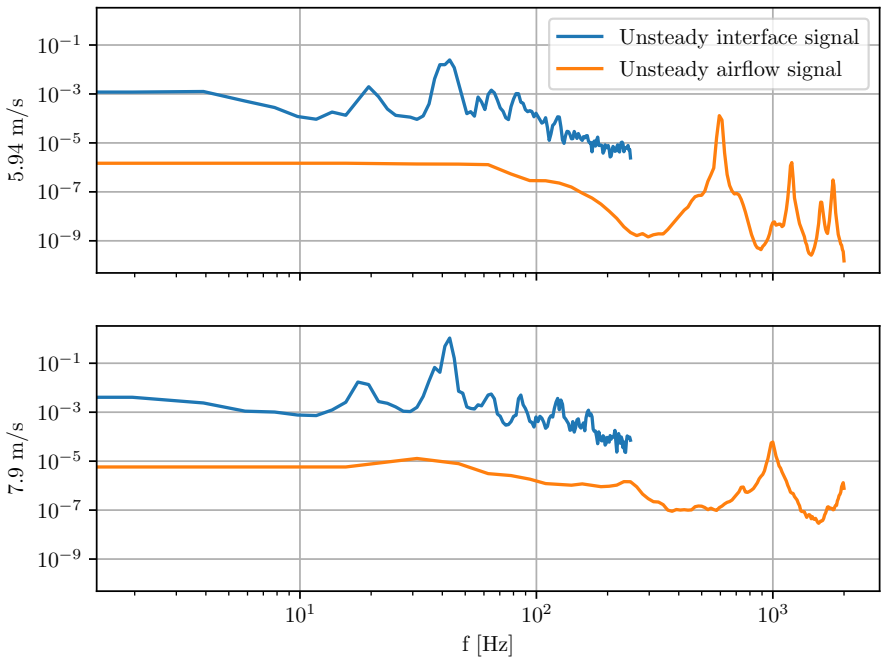

Figure 4.14: Unsteady signal power spectra for a 50 μL water drop at various freestream speeds.

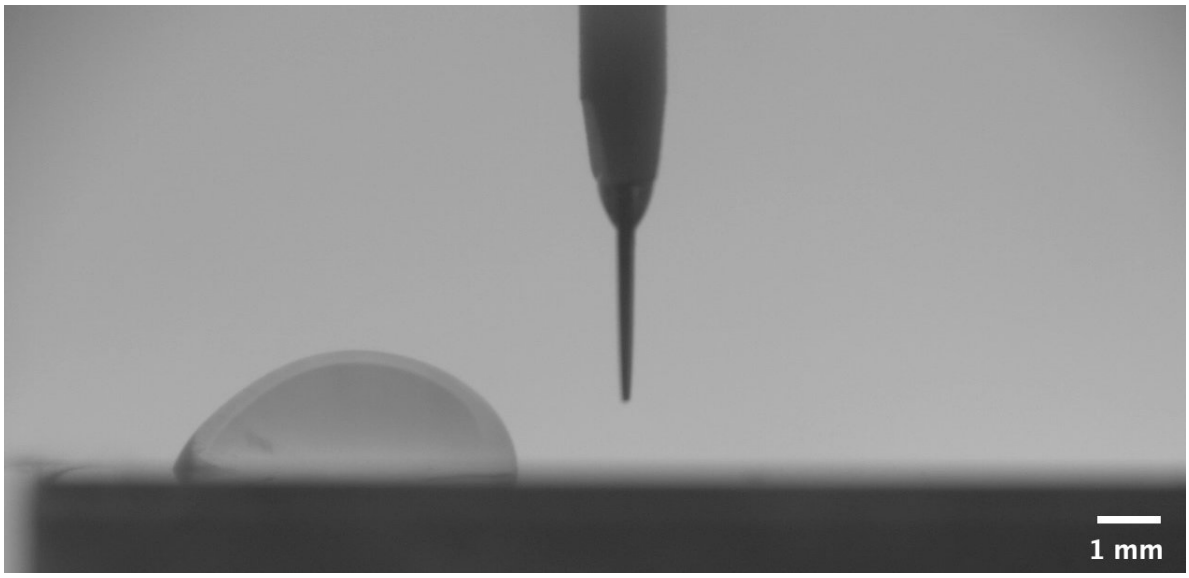

Figure 4.15: Shape of 75 μL water drop at 5.9 m/s and hotwire location relative to drop advancing side.

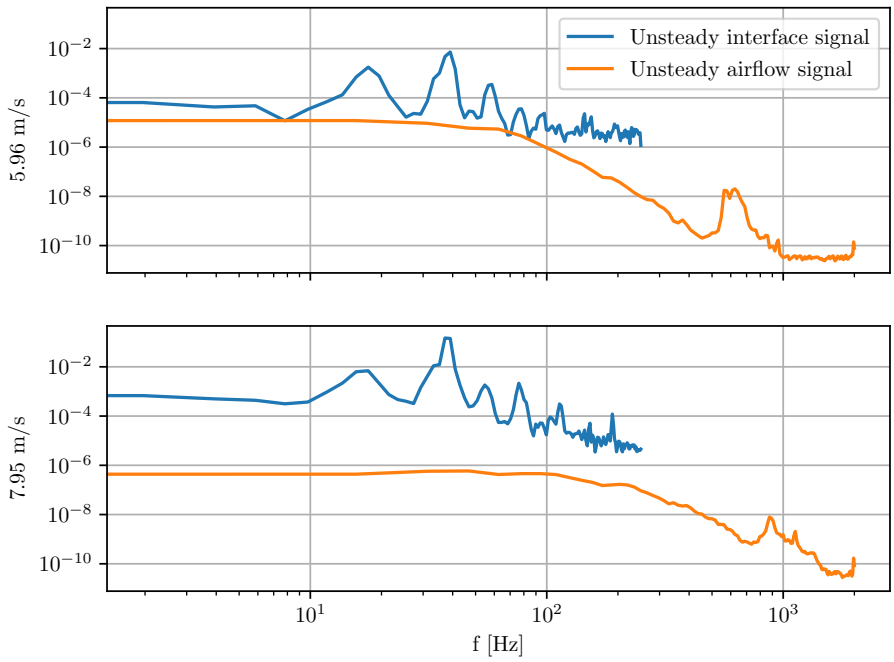

Figure 4.16: Unsteady signal power spectra for a 75 μL water drop at various freestream speeds.

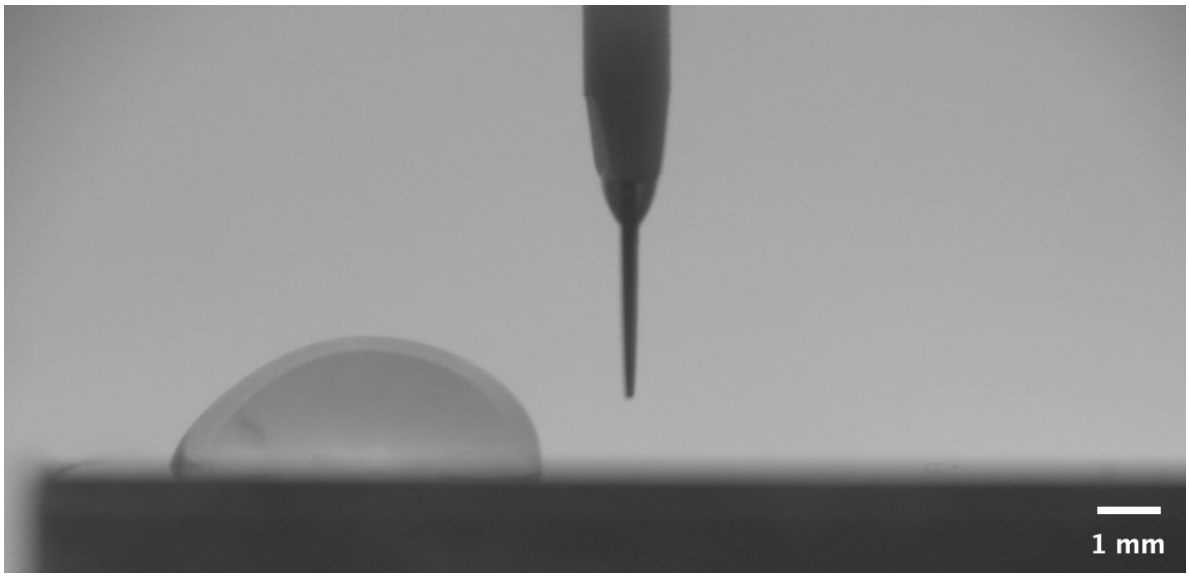

Figure 4.17: Shape of 100 μL water drop at 5.9 m/s and hotwire location relative to drop advancing side.

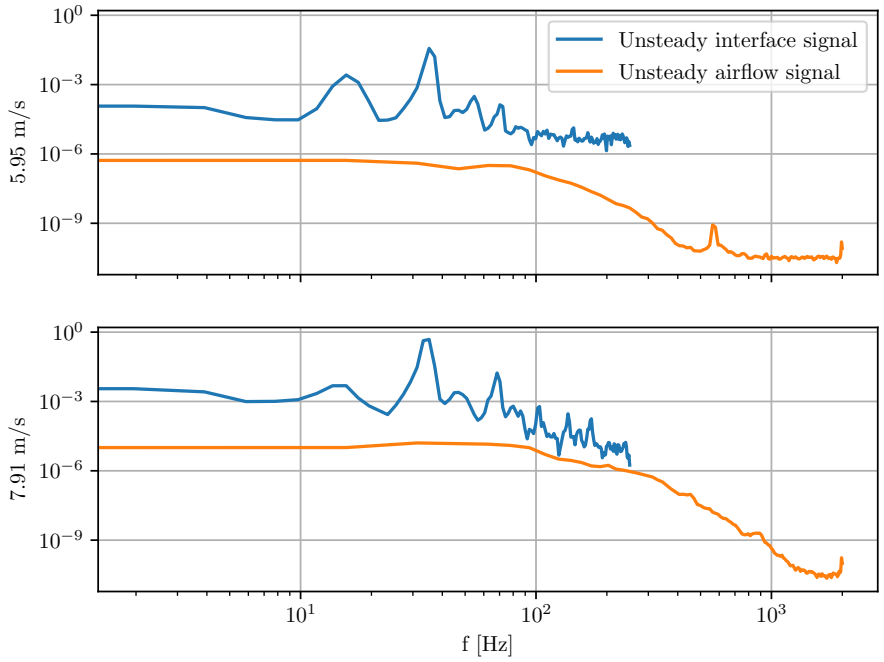

Figure 4.18: Unsteady signal power spectra for a 100 μL water drop at various freestream speeds.

4.3 Solid Hemisphere vs. Water Drop Comparison

In order to determine how airflow unsteadiness may depend on drop shape unsteadiness, the drop was replaced with a solid hemisphere with radius of 3.175 mm and an equivalent drop volume of 67 μL. The hotwire was placed approximately four diameters downstream of the hemisphere and at an elevated height of 2.38 mm.

For the hemisphere case, Figure 4.19 shows clear evidence of vortex shedding for various freestream speeds. St values are consistent with was found in [8]. Keeping the hotwire in the same position, a 67 μL water drop was placed on the surface. The result shown in Figure 4.20 are nearly identical to what was discovered for the solid case. Based on this data, the number of vortices shed downstream is not influenced by whether the protuberance is a solid or liquid and, by extension, drop oscillation.

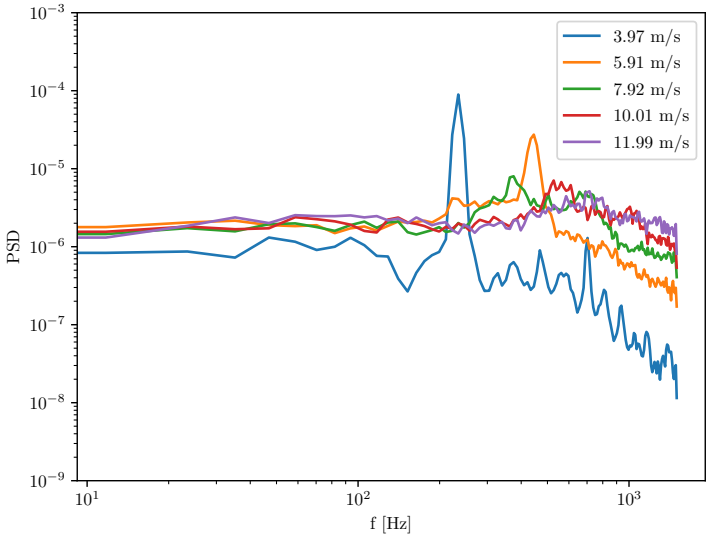

Figure 4.19: Airflow power spectra of a solid hemisphere at various freestream speeds. R = 3.175 mm.

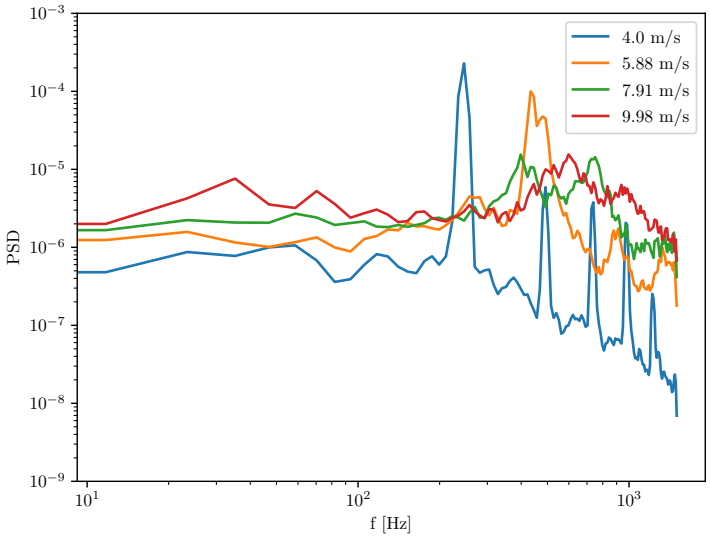

Figure 4.20: Airflow power spectra of a 67 μL water drop at various freestream speeds.

The results presented in this thesis conclude that there is not a coupling between near-wake airflow unsteadiness and drop interface oscillation. It was found that a drop will

oscillate at a frequency much lower than the near-wake airflow unsteadiness. Interface oscillation amplitude and vortex shedding amplitude will grow by small amounts as airflow speed increases. None of the results provide strong evidence that drops experience resonance just prior to depinning. More work will need to be done in the future to better understand this, but this thesis lays the foundation for how the drop stability problem can be studied in a different way than past work.

5. CONCLUSIONS

This thesis provides simultaneous measurements of unsteady interface shape and airflow fluctuations for various drop volumes. Due to vortex shedding being a much faster process than drop oscillation, time domain results did not provide any useful information. As Bond number increases, interface oscillation frequency will rapidly decrease until Bond number equals one and it will essentially remain constant beyond that point. Therefore, oscillation is tied extremely close to whether the drop is in a gravity- or surface tension-dominated flow field. Regardless of drop volume, the increase in flow speed has a direct relationship on oscillation amplitude. However, resonance was never observed.

Hotwire data showed there is a great challenge with placing the hotwire in a position sufficient enough to observe a wide range of frequencies present in a signal. Nonetheless, the hemisphere and water drop comparison showed that airflow unsteadiness downstream does not depend on drop oscillation.

This research focused on studying the drop depinning problem at zero inclination. In order to establish a greater understanding of drop behavior, different angles of attack will need to be considered. Only one aluminum surface was used for all of the experiments and this certainly has limitations. Studying drop oscillation on flat plates with varying surface roughness will provide more of a comprehensive look as well.

As discussed, the goal of this thesis was to provide a new way of studying drop depinning through the careful assessment of drop interface unsteadiness and vortex shedding in the separated drop wake. A synchronization technique was used in order to examine these two actions simultaneously. Promising results were yielded as a consequence of conducting a series of experiments. Surface tension and aerodynamic drag play a crucial role in drop oscillation and how these two interact should be further explored in order to establish a firm understanding of the fundamental, physical reason of why drops depin when they do.

REFERENCES

[1] J. Schmucker, "Experimental investigation of wind-forced drop stability," *Ph.D dissertation, Texas A&M University*, 2012.

[2] A. Milne and A. Amirfazli, "Drop shedding by shear flow for hydrophilic to superhydrophobic surfaces," *Langmuir*, vol. 25, pp. 14,155–14,164, 2009.

[3] S. Kandlikar and M. Steinke, "Contact angles and interface behavior during rapid evaporation of liquid on a heated surface," *J. Electrochem. Soc.*, vol. 153, pp. 225–232, 2006.

[4] F. Zhang, X. Yang, and C. Wang, "Liquid water removal from a polymer electrolyte fuel cell," *Int. J. Heat Mass Transfer*, vol. 45, pp. 3771–3780, 2002.

[5] M. Mahé, M. Vignes-Adler, P. Adler, and C. Jacquin, "Detachment of drops from flat solid surface by a simple shear flow," *J. Colloid Interface Sci.*, vol. 126, p. 329, 1988.

[6] A. Schleizer and R. Bonnecaze, "Displacement of a two-dimensional immiscible droplet adhering to a wall in shear and pressure-driven flows," *J. Fluid Mech.*, vol. 383, p. 29, 1999.

[7] E. White and J. Schmucker, "A runback criterion for water drops in a turbulent accelerated boundary layer," *J. Fluid Eng.*, vol. 130, p. 302, 2008.

[8] M. Acarlar and C. Smith, "A study of hairpin vortices in a laminar boundary layer," *J. Fluid Mech.*, vol. 175, p. 1–41, 1986.

[9] J. Bikerman, "Sliding of drops from surfaces of different roughnesses.," *J. Colloid Interface Sci.*, vol. 5, pp. 349–359, 1950.

[10] J. Fan, M. Wilson, and N. Kapur, "Displacement of liquid droplets on a surface by a shearing air flow," *J. Colloid Interface Sci.*, pp. 286–292, 2011.

[11] E. White and J. Schmucker, "Wind- and gravity-forced drop depinning," *arXiv:2009.04059v1 [physics.flu-dyn]*, 2020.

[12] P. Durbin, "On the wind force needed to dislodge a drop adhered to a surface," *J. Fluid Mech.*, vol. 196, pp. 205–222, 1988.

[13] P. Dimitrakopoulos and J. Higdon, "Displacement of fluid droplets from solid surfaces in low-reynolds-number shear flows," *J. Fluid Mech.*, vol. 336, pp. 351–378, 1997.

[14] P. Seiler, M. Gloerfeld, I. Roisman, and C. Tropea, "Aerodynamically driven motion of a wall-bounded on a smooth solid substrate," *Phys. Rev. Fluids*, vol. 4, p. 024001, 2019.

[15] J. Plateau, "Annual report of the board of regents of the smithsonian institution," *Government Printing Office*, vol. 1864, 1865.

[16] H. Rodot, C. Bisch, and A. Lasek, "Zero-gravity simulation of liquids in contact with a solid surface," *Acta Astronaut*, vol. 6, pp. 1083–1092, 1979.

[17] M. Strani and F. Sabetta, "Free vibrations of a drop in partial contact with a solid support," *J. Fluid Mech.*, vol. 141, p. 233, 1984.

[18] Y. Watanabe, "Free vibrations of a drop in partial contact with a circular support," *J. Appl. Phys.*, vol. 27, p. 2409, 1988.

[19] R. Smithwick and J. Boulet, "Vibrations of microscopic mercury droplets on glass," *J. Colloid Interface Sci.*, vol. 130, p. 588, 1989.

[20] D. Lyubimov, T. Lyubimova, and S. Shklyaev, "Non-axisymmetric oscillations of a hemispherical drop," *Fluid Dynamics*, vol. 39, pp. 851–862, 2004.

[21] H. Bauer and M. Chiba, "Oscillations of captured spherical drop of frictionless liquid," *J. Sound Vib.*, vol. 274, p. 725, 2004.

[22] M. Chiba, T. Miyazawa, and H. Baoyin, "Coupled free vibrations of a cantilever plate with attached liquid drop," *J. Sound Vib.*, vol. 298, p. 257, 2006.

[23] C. Bisch, "Les modes de vibrations axiales et tangentielles d'une sphère semi-libre," *C. R. Acad. Sci. II*, vol. 293, p. 107, 1981.

[24] M. Chiba, S. Michiue, and I. Katayama, "Free vibration of a spherical liquid drop attached to a conical base in zero gravity," *J. Sound Vib.*, vol. 331, p. 1908–1925, 2012.

[25] S. Sharma and D. Wilson, "Natural oscillations of a sessile drop: Inviscid theory," *arXiv:2010.14797v1 [physics.flu-dyn]*, 2020.

[26] A. Milne, B. Defez, M. Cabrerizo-Vílchez, and A. Amirfazli, "Understanding (sessile/constrained) bubble and drop oscillations," *J. Colloid Interface Sci.*, vol. 203, pp. 22–36, 2014.

[27] W. Möller, "Experimentelle untersunchung zur hydromechanik der kugel," *Z. Phys.*, vol. 39, pp. 57–80, 1938.

[28] H. Dryden, "Review of the published data on the effects of roughness on transition from laminar to turbulent flow," *J. Aero Sci.*, vol. 20, pp. 477–482, 1953.

[29] P. Klebanoff, "Measurements of the effect of two-dimensional roughness elements on boundary layer transition," *J. Aero Sci.*, vol. 15, pp. 803–804, 1955.

[30] I. Tani, "Effect of two-dimensional and isolated roughness on laminar flow," *Boundary Layer and Flow Control*, vol. 2, pp. 637–656, 1961.

[31] M. Mochizuki, "Hot-wire investigations of smoke patterns caused by a spherical roughness element," *Nat. Sci. Rep Ochanomizu University*, vol. 12, pp. 87–101, 1961.

[32] P. Klebanoff, K. Tidstrom, and L. Sargent, "The three-dimensional nature of boundary-layer stability," *J. Fluid Mech.*, vol. 12, pp. 1–34, 1962.

[33] G. Hall, "Interaction of the wake from bluff bodies with an initially laminar boundary layer," *AZAA J.*, vol. 5, pp. 1386–1392, 1967.

[34] S. Metzler, "Processes in the wall region of a turbulent boundary layer," *M.S. thesis, Lehigh University*, 1980.

[35] A. Johansson and P. Alfredsson, "On the structure of turbulent channel flow," *J. Fluid Mech.*, vol. 122, pp. 295–314, 1982.

[36] D. Marquardt, "An algorithm for least-squares estimation of nonlinear parameters," *J. Soc. Indust. Appl. Math.*, vol. 11, pp. 431–441, 1963.

[37] O. Solomon., "Psd computations using welch's method," 1991.